Petrov-Galerkin computation of nonlinear waves in pipe flow of shear-thinning fluids: first theoretical evidences for a delayed transition

Nicolas Roland, Emmanuel Plaut & Chérif Nouar

LEMTA, Nancy-Université & CNRS,
2 avenue de la Forêt de Haye, 54516 Vandœuvre cedex, France

Abstract

A pseudospectral Petrov-Galerkin code is developed in order to compute nonlinear traveling waves in pipe flow of shear-thinning fluids. The framework is continuum mechanics and the rheological model used is the purely viscous Carreau model. The code is validated, and a study of its convergence properties is made. It is shown that exponential convergence is obtained, despite the highly nonlinear nature of the viscous diffusion terms. Physical computations show that, as compared with the case of a constant-viscosity fluid, i.e., a Newtonian fluid, in the case of shear-thinning fluids the critical Reynolds number of the saddle-node bifurcation where the waves with an azimuthal wavenumber $m_0 = 3$ appear increases significantly when the non-Newtonian effects come into play.

Keywords: Pseudospectral methods, Pipe flow, Non-Newtonian fluids

1. Introduction

The study of the transition to turbulence in pipe flow of Newtonian and non-Newtonian fluids is an active area of research. The transition to turbulence has an impact on the head losses, which increase: delaying the transition could lead to a reduction of power consumption. From a more fundamental point of view, the interest of the scientific community in this subject could be explained by the fact that there are still mysteries and controversies running, see e.g. the recent study of the lifetime of turbulence in [1]. The difficulties with these studies, as far as modelling approaches are concerned, stem from the fact that the Hagen-Poiseuille base flow is linearly stable for all Reynolds number, see e.g. [2] and references therein. Hence standard stability methods cannot be used.

The same theoretical difficulty exists for non-Newtonian fluids, which are ubiquitous in nature and industry: blood, muds, paints, cement, polymer solutions are various examples of such fluids. Most of them exhibit two rather different types of non-Newtonian effects. Firstly, they are often shear-thinning: many of their flow properties can be described with a viscous model where the viscosity depends on the rate of strain (more precisely on the second invariant of the rate-of-strain tensor, see Eq. 5 below), decreasing when the rate of strain increases. Secondly, they may also display an elastic response to strain.

Experimentally, one can define the onset of the transition to turbulence in pipe flow as the Reynolds number at which the relative level I_T of fluctuations of the axial velocity v_z (the time-averaged value of $\sqrt{(v_z - \langle v_z \rangle_t)^2} / \langle v_z \rangle_t$, with $\langle v_z \rangle_t$ the time-averaged value of v_z), measured close to the wall, starts to increase significantly and quit the 'noise' value obtained in the laminar regime ($I_T \simeq 2 - 5\%$ depending on the setup and on the

measurement method). This increase is connected with the appearance, in an intermittent manner, of 'puffs'. In setups where no special care is taken to reduce perturbations, and when a Newtonian fluid is used, this Reynolds number $\overline{Re}$ (based on the mean flow speed $\langle v_z \rangle_{r\theta}$ and the pipe diameter) is of the order of 2000. On these topics, see e.g. [3, 4], and references therein. In non-Newtonian fluids, the relevant Reynolds number is the wall-viscosity Reynolds number $\overline{Re}_W$, defined in Eq. (32) below, and based on the viscosity at the wall deduced from the wall shear-stress. The onset of the transition to turbulence measured in the same way appears to be larger than 2000. The first ones to mention this delayed transition are, to our knowledge, [5]. In their article, p. 210, one can read that 'the onset of transition is slightly but progressively delayed in the sequence' of fluids 'by a factor of about two in Reynolds number', i.e. in some fluids transition comes in only for $\overline{Re}_W \gtrsim 4000$. The comparison of the curves I_T vs $\overline{Re}_W$ in the Fig. 3b, for a Newtonian fluid, and 5b, for a non-Newtonian fluid, of [6] also shows a clear delay to the transition in the latter case. A recent, spectacular example of delayed transition is given by the case of 0.125% PAA (an aqueous solution of polyacrylamide, of concentration 0.125% w/w) in the Fig. 4b of [7]: in this fluid the level of fluctuations I_T increases abruptly only for $\overline{Re}_W \gtrsim 8000$.

The interpretation of this delayed transition is not straightforward, since all fluids are both, to certain extent, shear-thinning and viscoelastic. Therefore it appears interesting to try to model this delayed transition with, for instance, a purely viscous constitutive law, in order to focus on the influence of the shear-thinning effects in the absence of elastic response. This is the aim of the work presented here.

As stated hereabove, one serious difficulty encountered in the modelling of the transition to turbulence in pipe flow is the fact

that the laminar base flow is linearly stable. One could use direct numerical simulations to attack the problem. At this stage we should mention the work of [8], who focused, however, on the transitional or turbulent regimes at large $\overline{Re}_W$, $\overline{Re}_W \gtrsim 5200$. We want to use here an alternate approach, which has emerged recently in the Newtonian studies.

Following the ideas of [9], developed for plane shear flows, it has been shown that nonlinear traveling wave solutions of the Navier-Stokes equation exist above a critical Reynolds number in pipe flow [10]. If (r, θ, z) designate the cylindrical coordinates with z the axial direction of the pipe, these solutions are invariant under the rotation $\theta \mapsto \theta + 2\pi/m_0$ with m_0 the fundamental azimuthal wavenumber, and under the translation $z \mapsto z + 2\pi/q_0$ with q_0 the fundamental axial wavenumber. Moreover they are invariant under the spatio-temporal translations $(z, t) \mapsto (z + \delta z, t + \delta t)$ provided that $\delta z = c\, \delta t$ with c the axial phase velocity. The Reynolds number at which these wave solutions appear, through a saddle-node bifurcation, could be viewed as a lower bound for the transition Reynolds number. Indeed, the transient turbulent states at intermediate Reynolds numbers, in the transitional regime, i.e., the 'puffs', would 'live' upon the manifold of such nonlinear wave solutions, see e.g. [11] and [12]. The relevant wave solutions have a fundamental azimuthal wavenumber $m_0 = 2, 3, 4, ...$ and appear at the critical Reynolds numbers $\overline{Re}_{c2} = 1359$, $\overline{Re}_{c3} = 1251$, $\overline{Re}_{c4} = 1647$, ... when defined with the mean flow speed $\langle v_z \rangle_{r\theta}$ and the pipe diameter. The corresponding Reynolds numbers defined with the centerline velocity of the base flow and the pipe radius are $Re_{c2} = 1663$, $Re_{c3} = 1631$, $Re_{c4} = 2280$, ... For each azimuthal wavenumber, the axial wavenumber has been determined by minimizing the critical Reynolds number $\overline{Re}$; for instance $q_0(m_0 = 2) = 1.55$, $q_0(m_0 = 3) = 2.44$ [13]. More recently, nonlinear wave solutions with $m_0 = 1$, which appear at lower Reynolds numbers $\overline{Re}_{c1,2} = 775$ and $\overline{Re}_{c1,1} = 820$, and present either two or one 'shift-and-reflect' symmetries (like the one defined in Eq. 28 below), have also been found [14, 15]. The role of these new solutions is not already quite clear. Some of them may support the 'boundary' between laminar and turbulent flow, see e.g. [16].

We present here a code that has been developed to compute, in the pipe flow of a shear-thinning fluid, nonlinear wave solutions of the first class found historically in the Newtonian case by [10, 13]. The model is presented in Section 2 and the numerical methods in Section 3. In Section 4, we present a validation of the code and a study of its convergence properties, by recovering a forced analytic solution. In Section 5, we present physical results for waves with $m_0 = 3$ and $q_0 = 2.44$, which are the first ones to emerge in this class in the Newtonian case. A concluding Section will follow.

2. Mathematical formulation

2.1. Carreau model. Basic equations with dimensional units

Since we focus on shear-thinning fluids without elastic response, the constitutive law is purely viscous: the stress tensor

$$\underline{\underline{\sigma}} = -p\underline{\underline{I}} + \underline{\underline{\tau}} \qquad (1)$$

with p the pressure and

$$\underline{\underline{\tau}} = \mu\underline{\underline{D}} \qquad (2)$$

the viscous-stress tensor. In Eq. (2), μ is the viscosity,

$$\underline{\underline{D}} = \underline{\underline{\nabla}}\mathbf{v} + \underline{\underline{\nabla}}\mathbf{v}^T \qquad (3)$$

is the rate-of-strain tensor, with $\mathbf{v}$ the velocity field. The constitutive law chosen is the Carreau's law, which has a firm theoretical base [17]. The viscosity

$$\mu = \mu(\Gamma_2) = \mu_\infty + (\mu_0 - \mu_\infty)\left(1 + \lambda^2\Gamma_2\right)^{(n_C-1)/2} \qquad (4)$$

with

$$\Gamma_2 = \frac{1}{2}\underline{\underline{D}} : \underline{\underline{D}} = \frac{1}{2}D_{ij}D_{ij} \qquad (5)$$

the second invariant of the rate-of-strain tensor, μ_0 the viscosity at zero strain, μ_∞ the viscosity at infinite strain, λ the characteristic time of the fluid, $n_C < 1$ the shear-thinning index. Note that in a unidirectional shear flow with velocity $\mathbf{v} = W(r)\,\mathbf{e}_z$, one has

$$\underline{\underline{D}} = \dot{\gamma}(\mathbf{e}_r \otimes \mathbf{e}_z + \mathbf{e}_z \otimes \mathbf{e}_r) \quad \text{with} \quad \dot{\gamma} = \frac{dW}{dr} \text{ the shear rate}, \quad (6)$$

hence

$$\Gamma_2 = \dot{\gamma}^2 \qquad (7)$$

and the relevant shear stress

$$\tau_{rz} = \mu\left(\dot{\gamma}^2\right)\dot{\gamma}. \qquad (8)$$

We use, as the flow variable controling the viscosity, Γ_2 instead of $\dot{\gamma} = \sqrt{\Gamma_2}$, because for three-dimensional flows this last quantity is singular if the strains vanish. Other shear-thinning constitutive laws are often used. The power-law model has for instance been used in [8]. This 2-parameters model is interesting because of its simplicity, but a drawback is that an infinite viscosity is obtained if the strains vanish, $\underline{\underline{D}} = \underline{\underline{0}}$. This leads to numerical problems in the corresponding flow regions, e.g., the pipe axis in pipe flow. On the contrary with the Carreau's law (4) the viscosity is a regular function of $\underline{\underline{D}}$ even at $\underline{\underline{D}} = \underline{\underline{0}}$. The 4-parameters model (4) can be considered as a special case of the 5-parameters Carreau-Yasuda model [18], which has for instance been used in [7] to reconstruct the rheological measurements for the three fluids used. Notice that, of the three fluids used in [7], 0.125% PAA can be well described by a Carreau model, as proves our Fig. 1. The dashed curve in Fig. 1 shows that, if, in the situations studied, the shear rates are not too high, a 3-parameters Carreau model with $\mu_\infty = 0$ could also be relevant.

The first equation to be solved is the linear momentum equation

$$\rho\left[\partial_t\mathbf{v} + \left(\underline{\underline{\nabla}}\mathbf{v}\right)\cdot\mathbf{v}\right] = -\boldsymbol{\nabla}p_{\text{tot}} + \mathbf{div}\underline{\underline{\tau}} \qquad (9)$$

where ρ is the density, and the total pressure p_{tot} contains the contribution of the gravitational force. The density ρ is assumed to be constant, i.e. the velocity field satisfies the incompressibility equation

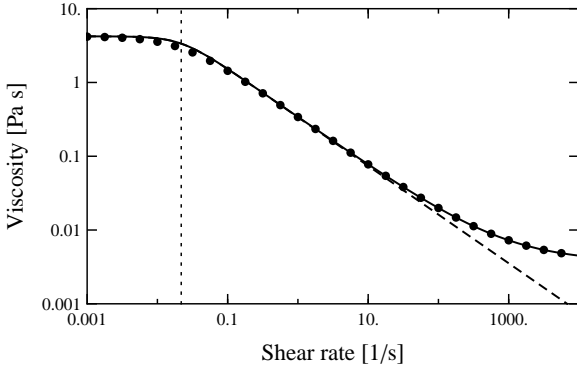$$\text{div}\mathbf{v} = 0. \qquad (10)$$

Figure 1: Flow curve μ vs $\dot{\gamma} = \sqrt{\Gamma_2}$ for the 0.125% PAA fluid studied by [7]. The disks show the result of the Carreau-Yasuda model, which is in perfect agreement with the rheological measurements (see the Fig. 2 of [7]). The continuous curve shows the result of the Carreau model (4), the parameters being $\mu_0 = 4.22$ Pa s, $\mu_\infty = 0.00372$ Pa s, $\lambda = 45.8$ s, $n_C = 0.34$. The dashed curve shows the result of the Carreau model with the same parameters except that $\mu_\infty = 0$. The dotted line shows the characteristic shear rate $\dot{\gamma} = 1/\lambda$ for the onset of shear-thinning.

2.2. Dimensionless units and parameters

From now on hats denote the dimensional quantities, to distinguish them from the dimensionless quantities. We will use, for the sake of simplicity, the Carreau model with

$$n_C = \frac{1}{2}, \tag{11}$$

which is considered to be a representative value of the shear-thinning index, and

$$\hat{\mu}_\infty = 0, \tag{12}$$

but these are not fundamental assumptions. Dimensionless variables are introduced. The velocity scale is a typical velocity $\hat{W}_0$ (the centerline velocity in the base flow for the physical computations, as it will be explained in Section 2.3), the length scale is the radius $\hat{a}$ of the pipe, the time scale is the advection time $\hat{t}_0 = \hat{a}/\hat{W}_0$, the viscosity scale is $\hat{\mu}_0$, the pressure and stress scale is $\hat{\rho}\hat{W}_0^2$. The dimensionless form of the Carreau's law (4) reads therefore

$$\mu = \left(1 + \lambda^2 \Gamma_2\right)^{-1/4} \tag{13}$$

with

$$\lambda = \frac{\hat{\lambda}}{\hat{t}_0} = \frac{\hat{\lambda}\hat{W}_0}{\hat{a}} \tag{14}$$

the 'non-Newtonian' number. The inverse of λ, $1/\lambda$, is the dimensionless shear rate for the onset of shear-thinning. The larger λ, the stronger the shear-thinning, non-Newtonian, effects; $\lambda = 0$ corresponds to a Newtonian fluid. The dimensionless viscous-stress tensor

$$\underline{\underline{\tau}} = Re^{-1} \mu \underline{\underline{\mathbf{D}}} \tag{15}$$

implies the Reynolds number

$$Re = \frac{\hat{W}_0 \hat{a} \hat{\rho}}{\hat{\mu}_0}. \tag{16}$$

Finally, the dimensionless form of Eq. (9) is

$$\partial_t \mathbf{v} + \left(\underline{\nabla}\mathbf{v}\right) \cdot \mathbf{v} = -\nabla p_{\text{tot}} + \mathbf{div}\underline{\underline{\tau}}. \tag{17}$$

2.3. Base flows

We recall that cylindrical coordinates (r, θ, z) are used. Except for the validation and convergence tests of Section 4, the flows are forced by a pressure field

$$p_{\text{tot}} = -Gz \tag{18}$$

with $G > 0$ the constant pressure gradient. This drives, using a laminar flow assumption, the base flow

$$\mathbf{v}_b = W_b(r)\,\mathbf{e}_z. \tag{19}$$

For this unidirectional flow, one is in the situation (6), (7), hence

$$\Gamma_2 = (W_b')^2, \tag{20}$$

denoting with a prime the derivative with respect to r. Therefore the viscosity

$$\mu_b = \left[1 + \lambda^2 (W_b')^2\right]^{-1/4}. \tag{21}$$

The momentum Eq. (17) yields, in the axial direction, the ODE

$$\alpha := Re\,G = -\frac{1}{r}\frac{d}{dr}(r\mu_b W_b'). \tag{22}$$

This ODE and the conditions

$$W_b(0) = 1, \quad W_b(1) = 0 \tag{23}$$

define the base flow and the product α between the Reynolds number and the pressure gradient, $\alpha = 4$ in the Newtonian case. In a dimensional setting, the first Eq. in (23) means that the typical velocity $\hat{W}_0$ is the centerline velocity in the base flow.

2.4. General assumptions concerning the wave solutions

The physical study of Section 5 will aim at computing non-linear wave solutions of (17) that are finite-amplitude perturbations of (18), (19),

$$p_{\text{tot}} = -Gz + \tilde{p} \tag{24}$$

and

$$\mathbf{v} = \mathbf{v}_b + \mathbf{u} \quad \text{with} \quad \mathbf{u} = u\mathbf{e}_r + v\mathbf{e}_\theta + w\mathbf{e}_z, \tag{25}$$

$\tilde{p}$, u, v, w depending on t only through $z - ct$ with c the phase velocity. It is also assumed that these 4 fields are periodic,

$$\theta \mapsto \theta + 2\pi/m_0 \quad \text{or} \quad z \mapsto z + 2\pi/q_0$$
$$\implies (\tilde{p}, u, v, w) \mapsto (\tilde{p}, u, v, w), \tag{26}$$

with $m_0 \in \mathbb{N}^*$ the fundamental azimutal wavenumber, $q_0 \in \mathbb{R}^*$ the fundamental axial wavenumber. The fact that the perturbation pressure field $\tilde{p}$ has no mean gradient in the axial direction corresponds to the hypothesis of a fixed pressure drop. The insertion of (24), (25) in (17) yields

$$\partial_t \mathbf{u} + W_b' u\,\mathbf{e}_z + W_b\,\partial_z \mathbf{u} + \left(\underline{\nabla}\mathbf{u}\right) \cdot \mathbf{u}$$
$$= -\nabla \tilde{p} + \mathbf{div}\underline{\underline{\tau}} - \mathbf{div}\underline{\underline{\tau}}_b \tag{27}$$

3

with $\mathbf{div}\overline{\overline{\boldsymbol\tau}}_b = -G\,\mathbf{e}_z$ the viscous term associated with the base flow. Eqs. (17) and (27) are equivalent, and in the next Section, for simplicity, we will refer only to (27).

Finally, it is assumed that the velocity fields $\mathbf{v}$ and $\mathbf{u}$ fulfill the symmetry property of the first waves found in the Newtonian case [10, 13], i.e. the 'shift-and-reflect' symmetry

$$(r,\,\theta,\,z) \;\mapsto\; (r,\,-\theta,\,z+\pi/q_0)$$
$$\Longrightarrow \quad (u,v,w) \;\mapsto\; (u,-v,w)\,. \qquad (28)$$

2.5. Wall-viscosity Reynolds number

In non-Newtonian fluids, it is questionable to use in the definition of the Reynolds number the viscosity $\hat{\mu}_0$, which is not always representative of the level of viscosities in the whole fluid domain. A more physical point of view is given by the consideration of the global momentum equation, for a laminar or nonlinear wave solution. The axial component of this equation shows a balance between the mean pressure gradient, which controls the head losses, and the tangential stress τ_{rz} averaged at the wall. Coming back, momentarily, to dimensional calculations, as show the hats, this equation reads

$$\hat{\tau}_{rzW} \;=\; \langle\hat{\tau}_{rz}(\hat{r}=\hat{a},\theta,\hat{z})\rangle_{\theta z} \;=\; -\frac{1}{2}\hat{G}\hat{a}\,. \qquad (29)$$

From an experimental point of view, the same balance is usually assumed to hold, even in a transitional regime, at least once a time-average has been taken. Experimentalists measuring $\hat{G}$ can therefore determine $\hat{\tau}_{rzW}$. From this shear stress and the rheological constitutive equation of the fluid, written under the form (8),

$$\hat{\tau}_{rzW} \;=\; \hat{\mu}\big((\hat{\dot\gamma}_W)^2\big)\,\hat{\dot\gamma}_W\,, \qquad (30)$$

they determine the 'wall shear rate' $\hat{\dot\gamma}_W$ and then the corresponding viscosity

$$\hat{\mu}_W \;=\; \hat{\mu}\big((\hat{\dot\gamma}_W)^2\big)\,, \qquad (31)$$

which is called the 'wall shear viscosity'. They define on the base of this viscosity and of the mean flow speed a wall-viscosity Reynolds number

$$\overline{Re}_W \;=\; \frac{\langle\hat{v}_z\rangle_{r\theta}\,\hat{d}\hat{\rho}}{\hat{\mu}_W} \qquad (32)$$

with $\hat{d}=2\hat{a}$ the pipe diameter [5, 6, 7]. This wall-viscosity Reynolds number is also the one that has been used in the numerical study [8]. In addition to arising naturally from the consideration of the mean pressure gradient, this Reynolds number has been shown to be the most relevant for stability analyses (in a channel geometry) by [19]. Importantly, the wall shear viscosity defined by (30), (31) is the viscosity at the wall in the laminar unidirectional flow solution that exists at the values of the parameters studied,

$$\hat{\mu}_W \;=\; \hat{\mu}_b(\hat{r}=\hat{a})\,. \qquad (33)$$

Turning back to dimensionless units, we note that the relation between the Reynolds numbers (16) and (32) reads

$$\overline{Re}_W \;=\; 2\,Re\,\frac{\langle v_z\rangle_{r\theta}}{\mu_W}\,. \qquad (34)$$

In the case of a Newtonian fluid we note $\overline{Re} = \overline{Re}_W$, since $\mu_W = 1$. If the flow is laminar (Hagen-Poiseuille flow), one has $\langle v_z\rangle_{r\theta} = 1/2$ and $\mu_W = 1$, hence $\overline{Re} = Re$. This simple relation breaks down, however, as soon as one considers nonlinear waves, since the mean flow speed departs from $1/2$. In the non-Newtonian case, even in the laminar regime, because of the parameter dependence of the base flows, one has $\overline{Re}_W \neq Re$. We shall come back to this in Section 5.1. We will also show in Section 5.2 that the nonlinear wave solutions found possess a viscosity field at the wall

$$\mu(r=1) \;\simeq\; \mu_W \qquad (35)$$

defined with the base flow. This relation, which will be precised numerically below (Tab. 2), justifies a posteriori the reasoning leading to (33).

3. Numerical methods

3.1. Spectral development

The Petrov-Galerkin formulation of [2, 20] has been used to solve Eqs. (10) and (27). The solutions are expanded as follows

$$\mathbf{u} \;=\; \sum_{l=-L}^{L}\sum_{m=-M}^{M}\sum_{n=1}^{N_r}\sum_{k=1}^{2} a_{l\,m\,n\,k}\mathbf{v}_{lq_0,mm_0,n,k}\,, \qquad (36)$$

with the trial fields, of the form

$$\mathbf{v}_{lq_0,mm_0,n,k} \;=\; \mathbf{V}_{lq_0,mm_0,n,k}(r)\exp\{i[mm_0\theta + lq_0(z-ct)]\}\,, \qquad (37)$$

given in Appendix A. The coefficients a_{lmnk} obey

$$a_{-l\,-m\,n\,k} \;=\; a^{*}_{l\,m\,n\,k} \qquad (38)$$

with the star designating the complex conjugate, in order for $\mathbf{v}$ to be real. This rule and the symmetry (28) impose some restrictions on the coefficients a_{lmnk}. Denoting by a^{r}_{lmnk}, a^{i}_{lmnk} the real and imaginary parts of a_{lmnk}, one has

$$\begin{aligned}
&\forall n, && a_{00n1}=0\,, \quad a^{i}_{00n2}=0\,, \\
&\forall n,\ \forall m\neq 0,\ \forall k, && a^{r}_{0mnk}=0\,, \quad a^{i}_{0\,-m\,n\,k}=-a^{i}_{0mnk}\,, \\
&\forall l\ \text{even}\neq 0,\ \forall n, && a_{l0n1}=0\,, \\
&\forall l\ \text{odd},\ \forall n, && a_{l0n2}=0\,,
\end{aligned}$$

$$\begin{aligned}
&\forall l\ \text{even}\neq 0,\ \forall m\neq 0,\ \forall n,\ \forall k, && a_{l\,-m\,n\,k}=-a_{lmnk}\,, \\
&\forall l\ \text{odd},\ \forall m\neq 0,\ \forall n,\ \forall k, && a_{l\,-m\,n\,k}=a_{lmnk}\,. \qquad (39)
\end{aligned}$$

Thus the velocity field depends only on the real coefficients a^{r}_{00n2}, a^{i}_{0mnk} for $m>0$, $a^{r,i}_{l0n1}$ for $l>0$ odd, $a^{r,i}_{l0n2}$ for $l>0$ even, $a^{r,i}_{lmnk}$ for $l>0$, $m>0$, which can be collected in a vector X of dimension

$$N_{\text{tot}} \;=\; (2L+1)\,(2M+1)\,N_r\,. \qquad (40)$$

4

3.2. Projection scheme

The trial fields being divergence-free, the only equation to solve is (27). Following [2, 20], this equation is projected onto test fields of the form

$$\widetilde{\mathbf{v}}_{lq_0,mm_0,n,k} = \widetilde{\mathbf{V}}_{lq_0,mm_0,n,k}(r)\exp\{i[mm_0\theta + lq_0(z - ct)]\}, \quad (41)$$

which are given in Appendix A, using the scalar product

$$\langle\, \mathbf{v} \,|\, \widetilde{\mathbf{v}} \,\rangle = \iiint_\Omega \mathbf{v} \cdot \widetilde{\mathbf{v}}^* \, r\, dr\, d\theta\, dz\,. \quad (42)$$

The integration domain

$$\Omega = \{(r,\theta,z) \in [0,1] \times [0, 2\pi/m_0] \times [0, 2\pi/q_0]\}\,. \quad (43)$$

Because all terms in (27) satisfy the 'shift-and-reflect' symmetry (28), and their projected coefficients obey the rules (39), this projection yields exactly N_{tot} real equations. These equations can be written

$$\mathbf{F}(X, Re) := c\mathbf{D}(X) + \mathbf{L}(X) + \mathbf{Q}_2(X) + Re^{-1}\,\mathbf{H}(X) = \mathbf{0}\,, \quad (44)$$

with $\mathbf{F}(., Re)$, $\mathbf{D}$, $\mathbf{L}$, $\mathbf{Q}_2$, $\mathbf{H}$ functions from $\mathbb{R}^{N_{tot}}$ to $\mathbb{R}^{N_{tot}}$. The linear operators $\mathbf{D}$ and $\mathbf{L}$ represent respectively $-\partial_z \mathbf{u}$ and $W_b' u\mathbf{e}_z + W_b\partial_z\mathbf{u}$. The quadratic operator $\mathbf{Q}_2$ represents $(\underline{\boldsymbol{\nabla}}\mathbf{u})\cdot\mathbf{u}$. The highly nonlinear operator $\mathbf{H}$ represents $\mathbf{div}(\mu\underline{\mathbf{D}} - \mu_b\underline{\mathbf{D}_b})$. Since the test fields vanish at the pipe wall and are periodic as the trial fields, for $\underline{\boldsymbol{\tau}}$ verifying the same periodicity rules (26) one has

$$\left\langle\, \mathbf{div}\underline{\boldsymbol{\tau}} \,\middle|\, \widetilde{\mathbf{v}} \,\right\rangle = -\iiint_\Omega \underline{\boldsymbol{\tau}} : \underline{\boldsymbol{\nabla}}\,\widetilde{\mathbf{v}}^* \, r\, dr\, d\theta\, dz\,. \quad (45)$$

Particularly the periodic pressure gradient term $-\boldsymbol{\nabla}\tilde{p}$ in Eq. (27) yields a contribution proportional to $\underline{\mathbf{I}} : \underline{\boldsymbol{\nabla}}\,\widetilde{\mathbf{v}}^*$ which vanishes since the test fields are divergence-free. The formula (45) is also used to calculate $\mathbf{H}$, which is therefore defined by a contribution proportional to $(\mu\underline{\mathbf{D}} - \mu_b\underline{\mathbf{D}_b}) : \underline{\boldsymbol{\nabla}}\,\widetilde{\mathbf{v}}^*$.

3.3. De-aliased pseudospectral method

A fast computation of the nonlinear terms in Eq. (44) is possible with a de-aliased pseudospectral method as described for instance in the Section 6.2 of [20]. A three-dimensional grid is introduced in the volume Ω, with Gauss-Lobatto points in the radial direction, regularly spaced points in the azimuthal and axial directions. The projected terms of Equation (27) are all even under $r \mapsto -r$, hence the radial integration can be performed with the Gauss-Lobatto quadrature formula retaining only the points in the interval $r \in\ ]0, 1[$, i.e.

$$r_j = \cos\left(\frac{j\pi}{NG_r}\right) \text{ for } j = 1, \cdots, \frac{NG_r - 1}{2},$$

with

$$NG_r = 3N_r + 8 \text{ if } N_r \text{ is odd}, \ 3N_r + 7 \text{ if } N_r \text{ is even}.$$

This number has been determined by requiring that the Gauss quadrature formula is exact for the projection of the nonlinear term $(\underline{\boldsymbol{\nabla}}\mathbf{u})\cdot\mathbf{u}$ in Equation (27); moreover NG_r is chosen odd to avoid having a point at $r = 0$, and to be able to use differenciation matrices to evaluate the radial derivatives of $\mathbf{u}$. The number of azimuthal points

$$NG_\theta = 3M + 2 \text{ if } M \text{ is odd}, \ 3M + 3 \text{ if } M \text{ is even},$$

the number of axial points

$$NG_z = 3L + 2 \text{ if } L \text{ is odd}, \ 3L + 3 \text{ if } L \text{ is even},$$

are dictated by the de-aliasing rule; besides, for the differenciation matrices used to evaluate the azimuthal and axial derivatives of $\mathbf{u}$, one wants an odd number of grid points. In practice, a partial summation technique is used to compute $\mathbf{u}$ at the grid points from the spectral expansion coefficients a_{lmnk}, and then differenciation matrices are used to compute $\underline{\boldsymbol{\nabla}}\mathbf{u}$. Relevant quantities like $(\underline{\boldsymbol{\nabla}}\mathbf{u})\cdot\mathbf{u}$ and $\mu\underline{\mathbf{D}}$ can then be obtained on the spatial grid. The projection integrals (42) are computed with Gauss quadrature formula in the radial direction, trapezoidal rules in the azimuthal and axial directions.

3.4. Phase condition to set the phase velocity

The physical wave solutions have a phase velocity that is not a free parameter, but is determined by the advection by the mean flow. In fact, a phase condition must be added to the Eqs. (44) to prevent the solutions from drifting in the pipe, as a result of the translational invariance in the axial direction of the physical Eq. (27). We have chosen the phase condition

$$\phi(X) = \sum_{n=1}^{N_r} a^r_{11n1}\mathbf{V}_{q_0,m_0,n,1}(r = 0.1) \cdot \mathbf{e}_r = 0\,. \quad (46)$$

The physical calculations will thus aim at computing the vector

$$\overline{X} = \begin{pmatrix} X \\ c \end{pmatrix} \quad (47)$$

solution of

$$\overline{F}(\overline{X}, Re) := \begin{pmatrix} F(X, Re) \\ \phi(X) \end{pmatrix} = \begin{pmatrix} \mathbf{0} \\ 0 \end{pmatrix}\,. \quad (48)$$

3.5. Newton-GMRES method

For the validation and convergence tests with a fixed phase velocity c, one has to solve Eq. (44) to determine X; for the physical wave computations, one has to solve Eq. (48) to determine X and c. In both cases this is done with a Newton method. Since the function ϕ (46) depends linearly on $\mathbf{X}$, it is simple to augment a method solving (44) in order to solve (48). For clarity reasons, we will only describe hereafter the method used to solve (44), by considering a case where c is fixed. The more general case with c unknown can be treated by replacing in what follows X by $\overline{X}$ and F by $\overline{F}$, and correcting in accordance the discussion on $\nabla_X F$. We also only describe hereafter a case where Re is fixed, postponing the evocation of a more general method where Re is variable to the next subsection.

We start with a guess value X_0 of X not too far from the solution at the parameters studied (the determination of X_0 will be explained in Sec. 3.6). At the iteration $j + 1$ of the Newton method, the computation of X_{j+1} from X_j requires in principle the knowledge of the gradient of F, to solve

$$\nabla_X F(X_j, Re) \cdot (X_{j+1} - X_j) = -F(X_j, Re) . \qquad (49)$$

Formally

$$\nabla_X F = cD + L + \nabla_X Q_2 + Re^{-1} \nabla_X H . \qquad (50)$$

The operators D and L are constant and simple; they are represented by matrices. On the contrary computing the full matrices representing the gradients of Q_2 and H is a quite long task, which should be avoided, or at least not be done at each iteration, especially concerning H which is highly nonlinear. For this reason a GMRES method [21] is used to solve (49). The restarted version of GMRES, the algorithm 4 of [21] is used, with a restart every 60 steps if convergence has not been obtained before. The criterion of convergence is the choice 2 of the 'inexact Newton method' of [22], with $\gamma = 1$ and the exponent $\alpha = 1.6$. The action of $\nabla_X H$ on the vectors implied in the GMRES method is done with a finite difference formula of order 4. Note also that, instead of a Gram-Schmidt process, Householder transformations are used in the GMRES method, following [23]. To accelerate the convergence of the GMRES method, the preconditioner

$$P = cD + L + \nabla_X Q_{2\mathrm{old}} + Re^{-1} H'_{\mathrm{old}} \qquad (51)$$

is applied to the system (49). The indexes 'old' mean that it is not computed at each Newton iteration, but typically every 5 Newton iterations. Moreover H' is the operator that represents

$$\mathbf{div}\big(\mu_{\mathrm{old}} \underline{\mathbf{D}}\big) . \qquad (52)$$

It corresponds to one contribution to $\nabla_X H$; other contributions also exist, where the viscosity has to be varied. Right preconditioning of the system (49) with the operator P defined by (51), which is stored and used with a LU decomposition, appears to be efficient. The criterion of convergence of the Newton method is

$$\|X_j - X_{j-1}\|_2 < 10^{-8} \ \text{ or } \ \|F(X_j, Re)\|_2 < 10^{-14} . \qquad (53)$$

If the first inequality stops the Newton iterations, it is checked that $\|F(X_j, Re)\|_2$ is small; typically $\|F(X_j, Re)\|_2 \lesssim 10^{-10}$.

3.6. Continuation method - Euler predictor

For the test computations of Sec. 4, the guess value X_0 is a simple perturbation of the real solution, which is known, see Eq. (63) below. For the physical computations of Sec. 5, the situation is more complicated since the solutions are unknown, and the solution branches can present bifurcation points. The pseudo-arc length method of [24] is used to follow the solutions in the parameter space, starting at the very beginning from Newtonian solutions obtained with the intermediate forcing method of [13]. In the pseudo-arc length method, Re is

treated as a parameter, and to pass from a numerical solution (X_s, Re_s) to another one on the solution branch on uses first an Euler predictor formula,

$$(X_0, Re_0) = (X_s, Re_s) + \delta s \left(\frac{dX}{ds}, \frac{dRe}{ds}\right) . \qquad (54)$$

In this equation δs is the curvilinear abscissa increment, whereas the tangent to the solution branch is computed by solving

$$\nabla_X F(X_s, Re_s) \cdot \frac{dX}{ds} + \nabla_{Re} F(X_s, Re_s) \cdot \frac{dRe}{ds} = 0 \qquad (55)$$

together with a normalization condition. The system (55) is also solved with a preconditioned GMRES method. The Newton method that follows has a variable Re; it is the modified Newton-GMRES method of [25]. An automatic control of the curvilinear abscissa increment δs is done, with criteria based on the variations of the vector $\left(\frac{dX}{ds}, \frac{dRe}{ds}\right)$.

3.7. Numerical performances

The code is written in Fortran 95 and runs on PCs, Intel Xeon 5160 at 3.00 GHz. A typical run for physical computations, to obtain the results that will be presented in Sec. 5, with truncation levels $(L, M, N_r) = (7, 10, 30)$, takes around 45 minutes to pass from one solution to the next one on the solution branch. The peak of RAM use, reached during the GMRES computations, is of the order of 4.5 Gb. An underestimation of the order of magnitude of the RAM needed can be obtained by considering that 5 large matrices of $N_{\mathrm{tot}} \times N_{\mathrm{tot}}$ double-precision floating numbers (the matrices P, D, L, $\nabla_X Q_{2\mathrm{old}}$ and H'_{old} of Equation 51) have to be stored.

4. Validation and convergence tests

In order to test the code, we have performed consistency tests similar to the ones exposed in the Section 4 of [26]. The analytical solution

$$
\begin{aligned}
u_a &= \frac{1}{2} r^2 (1 - r^2)^2 \cosh r \ \sin\theta \ \sin(z - t/2) , \\
v_a &= \frac{1}{2} r^2 (r^2 - 1) \Big[(7r^2 - 3) \cosh r + \\
&\quad r \sinh r \ (r^2 - 1 + 2r \sinh r) \Big] \cos\theta \ \sin(z - t/2) , \\
w_a &= r^3 (1 - r^2) \sinh^2 r \ \sin\theta \ \cos(z - t/2) \qquad (56)
\end{aligned}
$$

has been forced in a case without pressure gradient ($G = 0$) and base flow ($\mathbf{v}_b = \mathbf{0}$). A forcing term

$$\mathbf{F}_a = -\tfrac{1}{2}\partial_z \mathbf{v}_a + \left(\underline{\nabla}\mathbf{v}_a\right) \cdot \mathbf{v}_a - Re^{-1}\mathbf{div}\big(\mu_a \underline{\mathbf{D}}_a\big) \qquad (57)$$

has been calculated by computing firstly the coefficients X_a of the spectral development of $\mathbf{v}_a$ and secondly $\mathbf{F}_a = F(X_a, Re)$. Whereas $\mathbf{v}_a$ is only rich in radial modes, and corresponds to $q_0 = l = 1$, $m_0 = m = 1$ only, $\mathbf{F}_a$ is rich in modes in all spatial directions, because of the nonlinear nature of μ_a. This is especially true if the Reynolds number is not too large. Since the
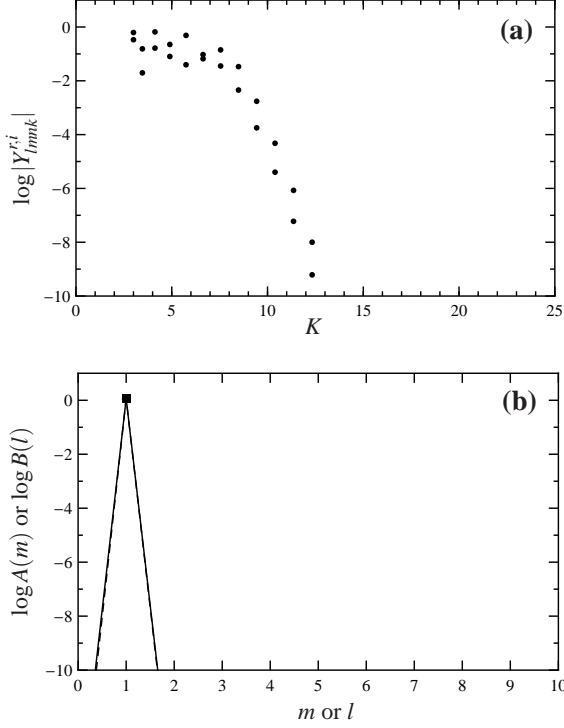
Figure 2: Spectrum of the coefficients $Y_{lmnk}^{r,i}$, the real and imaginary parts of $\langle \mathbf{v}_a \mid \widetilde{\mathbf{v}}_{l,m,n,k} \rangle$, computed with $N = 19$ (see Eq. 65). (a) : Decimal logarithms of the 24 coefficients $|Y_{lmnk}^{r,i}| > 10^{-10}$ vs the generalized wavenumber K defined by Eq. (58). (b) : The disks (resp. squares) show $\log A(m)$ vs m (resp. $\log B(l)$ vs l) with the amplitudes defined by Eqs. (59) and (60). In this case, since there is energy only on the modes $m = l = 1$, one has $A(1) = B(1)$, $A(m) < 10^{-14}$ for $m \neq 1$, $B(l) < 10^{-14}$ for $l \neq 1$.

novelty of our code is precisely the encoding of $\mathbf{div}\mu\underline{\underline{\mathbf{D}}}$ with a nonlinear viscosity μ given by (13), we have chosen to perform our first tests at $Re = 10$. The comparison of the spectrum of Y_a, the real and imaginary parts of $\langle \mathbf{v}_a \mid \widetilde{\mathbf{v}}_{l,m,n,k} \rangle$ for $l, m, n, k \geq 0$, shown in Fig. 2, and of the spectrum of F_a, shown in Fig. 3, demonstrates the richness of the latter. In the upper graphs of these two Figures, the generalized wavenumber

$$K = \sqrt{(l+1)^2 + (m+1)^2 + n^2} \qquad (58)$$

has been used to index the coefficients in a manner representing the 'degree of oscillations' in all spatial directions of the associated test fields. In the lower graphs, the quantities

$$A(m) = \sqrt{\sum_{l,n,k}[(a_{lmnk}^r)^2 + (a_{lmnk}^i)^2]}, \qquad (59)$$

$$B(l) = \sqrt{\sum_{m,n,k}[(a_{lmnk}^r)^2 + (a_{lmnk}^i)^2]}, \qquad (60)$$

with a_{lmnk} designating, here, one projection integral, are used, in order to show the 'energy' associated with a particular wavenumber.

Independently of the Fortran computations, a calculation of F_a has been realized with Mathematica, through a formal computation of $\mathbf{F}_a$ followed by a numerical computation of some

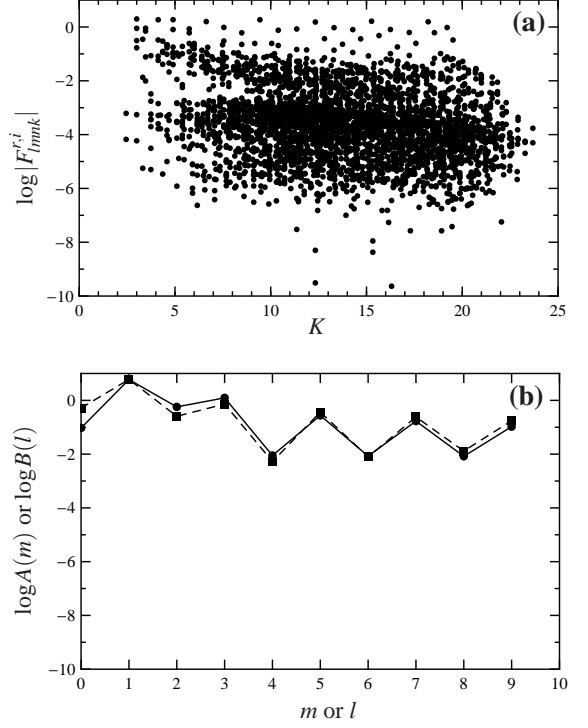Figure 3: For $Re = 10$, $\lambda = 4$, spectrum of the coefficients $F_{lmnk}^{r,i}$ that constitute F_a computed with $N = 19$ (see Eq. 65). (a) : Decimal logarithms of the 3399 coefficients $|F_{lmnk}^{r,i}| > 10^{-10}$ vs the generalized wavenumber K. (b) : The disks (resp. squares) show $\log A(m)$ vs m (resp. $\log B(l)$ vs l).

projection coefficients $\langle \mathbf{F}_a \mid \widetilde{\mathbf{v}}_{l,m,n,k} \rangle$ for some values of l, m, n and k. The relative errors between the integrals obtained with Mathematica and the corresponding components of F_a computed with the fully numeric Fortran code are smaller than $4\ 10^{-6}$.

With the Fortran code, the forced momentum equation

$$\partial_t \mathbf{v} + \left(\underline{\underline{\nabla}}\mathbf{v}\right) \cdot \mathbf{v} = -\nabla\tilde{p} + Re^{-1}\mathbf{div}\left(\mu\underline{\underline{\mathbf{D}}}\right) + \mathbf{F}_a, \qquad (61)$$

represented by

$$\mathbf{F}(X, Re) - \mathbf{F}_a = \mathbf{0}, \qquad (62)$$

has been solved with the Newton-GMRES method, starting from the initial condition

$$X_0 = X_a + \tfrac{1}{100}X_p. \qquad (63)$$

In this equation, X_p is the spectral development on the base of the trial fields of the solenoidal vector field

$$u_p = \cos\theta, \quad v_p = -\sin\theta, \quad w_p = r\cos\theta. \qquad (64)$$

Convergence of the solution towards a fixed point X_∞ quite close to X_a is obtained, and a discrete L2-error on the spatial grid points between the corresponding field $\mathbf{v}_\infty$, computed numerically, and the analytical field $\mathbf{v}_a$ has been computed. This test has been performed with various values of N, the number of real modes in each direction, i.e., according to Eq. (40),

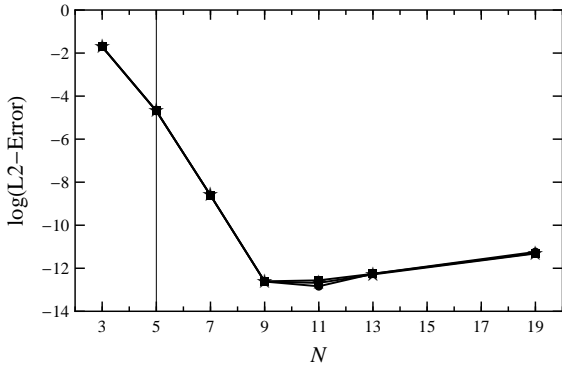$$N = 2L + 1 = 2M + 1 = N_r. \qquad (65)$$

7

Figure 4: Decimal logarithm of the L2-error vs the number of modes N (65) for a consistency test where the analytic solution (56) has been forced. The parameters are $Re = 10$ and $\lambda = 0$ (disks), 1 (squares), 4 (stars).
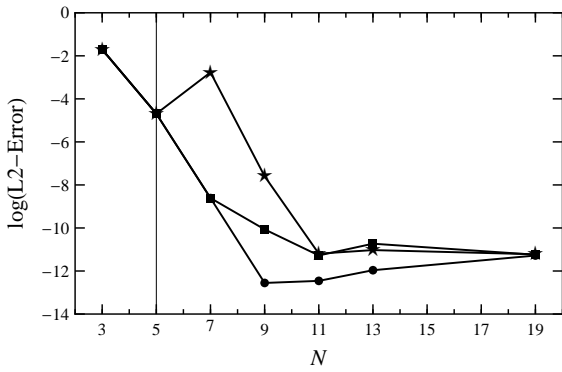

Figure 5: Same as Fig. 4, but for $Re = 1000$.

The Fig. 4 has been obtained, which proves that exponential convergence occurs, even in the non-Newtonian cases ($\lambda > 0$), despite the highly-nonlinear nature of the viscous terms in Eq. (61). Another test has been performed at a higher value of the Reynolds number, $Re = 1000$. Fig. 5 has been obtained, which shows that for $\lambda > 0$ one does not always converge to $X_\infty = X_a$. However exponential convergence still occurs, though in a slower manner, especially for the case $\lambda = 4$ of a strongly shear-thinning fluid.

5. Physical results

5.1. Base flows

For a given non-Newtonian fluid and pipe diameter, setting λ given by Eq. (14) amounts to set the characteristic velocity

$$\hat{W}_0 = \frac{\hat{a}}{\hat{\lambda}} \lambda. \tag{66}$$

The Reynolds number (16) is also set to

$$Re = \frac{\hat{\rho} \, \hat{a}^2}{\hat{\mu}_0 \, \hat{\lambda}} \lambda. \tag{67}$$

This Reynolds number is a 'pressure-gradient Reynolds number', since, according to the model described in Section 2.3, all
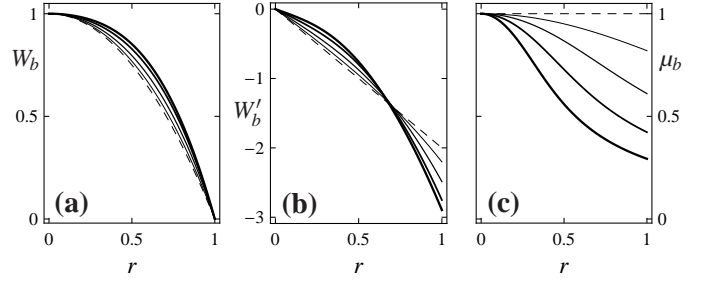

Figure 6: Base flow functions vs the cylindrical radius r. The dashed line shows the Newtonian case $\lambda = 0$, the continuous lines of increasing thickness show the cases $\lambda = 0.5$, 1, 2 and 4. (a) : Axial velocity. (b) : Shear-rate. (c) : Viscosity.

λ	$\langle W_b \rangle_{r\theta}$	μ_W	$1/\mu_W$	α	$\alpha \lambda$
0	0.500	1	1	4	0
0.5	0.517	0.8199	1.220	3.611	1.806
1	0.541	0.6107	1.637	3.038	3.038
2	0.567	0.4228	2.365	2.327	4.654
4	0.585	0.2933	3.410	1.699	6.794

Table 1: Properties of the base flows for various values of λ.

flows are controlled by the applied pressure gradient

$$\hat{G} = \frac{\hat{\rho} \, \hat{W}_0^2}{\hat{a}} G = \frac{\hat{\rho} \, \hat{W}_0^2}{\hat{a}} \frac{\alpha}{Re} = \frac{\hat{\mu}_0}{\hat{a} \, \hat{\lambda}} \alpha \lambda. \tag{68}$$

For the purpose of completeness, we show in Fig. 6 the base flows W_b, the corresponding shear-rates W_b' and the viscosities μ_b for various values of λ. They have been obtained through a numerical solution of the problem (22), (23). When λ increases, $|W_b'(r = 1)|$ increases only slightly, whereas $\mu_W = \mu_b(r = 1)$ decreases strongly, hence

$$\alpha = - \frac{d}{dr} (r \mu_b W_b') \Big|_{r=1} \tag{69}$$

decreases, as shown in the Tab. 1. The last column of this Table shows that the dimensional pressure gradient needed to sustain the base flow increases significantly when λ increases; note that the Eqs. (66) to (68) are not valid for a Newtonian fluid ($\lambda = 0$).

5.2. Nonlinear waves

As stated in the introduction, we focus on the case of the waves found by [10, 13] in Newtonian fluids that display the lowest critical Reynolds number $\overline{Re}$. These waves correspond to an axial wavenumber $q_0 = 2.44$ and an azimuthal wavenumber $m_0 = 3$. Selecting these values of the geometrical parameters, we have first recovered (with the intermediate forcing method of [13]) the Newtonian solutions for $\lambda = 0$, which constitutes another validation of our code. Thus the dashed curve in our Fig. 7 corresponds to the lowest curve in the Fig. 7 of [13]. We have then increased the non-Newtonian parameter λ by steps, and followed by continuation the solution branches. In the (Re, c) plane, as shown in Fig. 7, first for $\lambda \lesssim 1$ the non-Newtonian waves appear at lower Re than for $\lambda = 0$, but then, for $\lambda \gtrsim 1$, the non-Newtonian waves appear at higher Re. A simpler picture is obtained, however, if
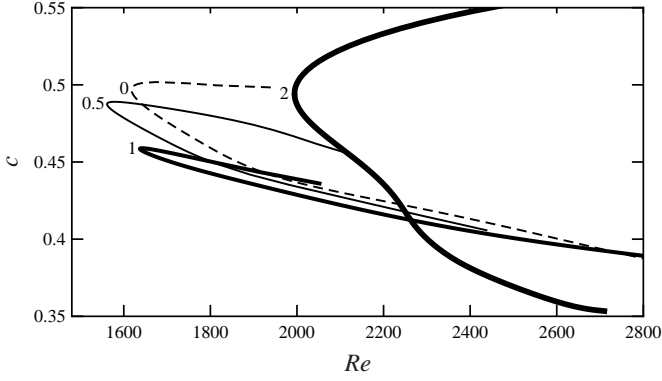
Figure 7: Phase velocities of nonlinear waves vs the pressure gradient Reynolds number for $m_0 = 3$, $q_0 = 2.44$. The dashed line shows the Newtonian case $\lambda = 0$, the continuous lines of increasing thickness show the cases $\lambda = 0.5$, 1 and 2. The values of λ are displayed to the left of the saddle-node points.
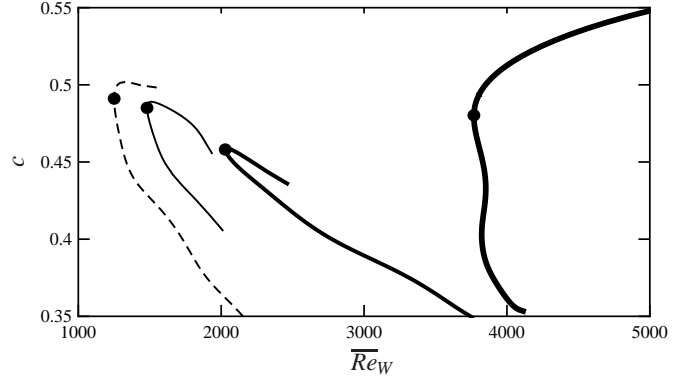

Figure 8: Same as Figure 7, except that the wall-viscosity Reynolds number (34) is used. The disks denote the saddle-node points, which define the critical waves.

Figure 9: Convergence test for $\lambda = 2$. The continuous curve has been computed with the truncation levels indicated in Tab. 2, $(L, M, N_r) = (7, 10, 30)$. The dotted curve has been computed with lower truncation levels, $(L', M', N'_r) = (5, 8, 24)$.

one uses the Reynolds number $\overline{Re}_W$, more relevant for non-Newtonian fluids, as the main parameter. As explained in Sec. 2.5, this Reynolds number is the wall-viscosity Reynolds number (34), $\overline{Re}_W = 2Re \langle v_z \rangle_{r\theta} / \mu_W$. Because the factor $1/\mu_W$ increases rapidly with λ, as shown in the fourth column of Tab. 1, whereas the mean flow speed $\langle v_z \rangle_{r\theta}$ remain roughly constant ($\langle v_z \rangle_{r\theta} \simeq 0.39$), the onset of the waves is clearly delayed when considered in terms of $\overline{Re}_W$: compare Fig. 7 and 8. Note that the Newtonian, dashed curve in Fig. 8 corresponds to the leftmost curve in the Fig. 10 of [13]. From now on we denote as 'critical waves' the waves that appear at the lowest values of $\overline{Re}_W$. The results of our Fig. 8, which are complemented by the Tab. 2, clearly show a tendency to delay the transition as the non-Newtonian parameter λ increases. In Tab. 2, the sixth column shows the averaged viscosity at the wall in the critical wave solutions: it coincides with the wall-viscosity μ_W (33) of the laminar flow (the third column of Tab. 1) within 1.4%. Nevertheless, the fluctuations of the viscosity at the wall are non-negligible, as shown in the seventh column of Tab. 2, which displays the maximum difference between the viscosity at the wall, computed at the grid points, and the averaged viscosity at the wall,

$$\delta\mu_W = \max_{\theta,z} \left| \mu(r = 1, \theta, z) - \langle \mu(r = 1, \theta, z) \rangle_{\theta z} \right|. \tag{70}$$

All the computations in Fig. 7 and 8 have been performed with the truncation levels (L, M, N_r) specified in the last column of Tab. 2. Convergence tests have been made to verify that computations with lower truncation levels (L', M', N'_r) such that

$$L' \leq L - 2, \quad M' \leq M - 2, \quad N'_r \leq N_r - 2,$$

give quite similar curves. Such a convergence test is displayed in Fig. 9. Note that, because of Eq. (40), the number of real modes increases from $N_{\text{tot}} = 4488$ to $N_{\text{tot}} = 9450$ between the two truncation levels used. The variations of the Reynolds numbers at the saddle-node points in the $(\overline{Re}_W, c)$ plane obtained with the different truncation levels have been used to estimate the error bars in the Tab. 2. At this stage it is interesting to consider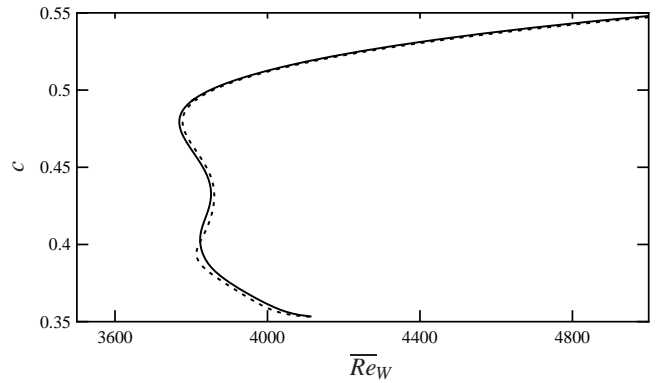, as shown in Figs. 10 and 11, the spectra of the critical waves. One observes, in Figs. 10a and 11a, a decrease of more than 4 order of magnitudes between the largest coefficients with $K \simeq 1$ and $K \simeq 30$, which confirms that the solutions are well converged. In Figs. 10b and 11b one also observes a decrease of the energy with increasing m and l. One remarks in Fig. 10b, for $\lambda = 0$, that one has $A(2) > A(1)$, which means that there is more energy on the modes in $\exp(\pm 6i\theta)$ than on the modes in $\exp(\pm 3i\theta)$. The Fig. 11b shows that this is is not the case for $\lambda = 2$.

The velocity field of these nonlinear waves can be visualized in a simple way if one averages it in the axial direction, as [10] and [13] did it. In most of their Figures, they substracted a laminar flow with the same mass flux to this mean flow (see the Eq. 5.2 of [13]). This procedure has a meaning in a Newtonian fluid, where the laminar flow is always given by the same parabolic function. On the contrary in a non-Newtonian fluid the laminar flow depends on the parameters, and it seems more relevant to consider either the total mean flow, i.e. $\langle \mathbf{v} \rangle_z$, or the mean flow minus the laminar base flow, i.e. $\langle \mathbf{u} \rangle_z$. The corresponding fields are displayed in Fig. 12. The scales of all the plots are defined by the columns 8 to 11 in Tab. 2. On the plots of $\langle v_z \rangle_z$ (left column of Fig. 12), one observes a classical effect due to the shear-thinning: the streamwise velocity tends

9

λ	$\overline{Re}_W$	Re	c	$\langle v_z \rangle_{r\theta}$	$\langle \mu(r=1) \rangle_{\theta z}$	$\delta\mu_W$	$\max \langle v_z \rangle_z$	$\max \langle w \rangle_z$	$\min \langle w \rangle_z$	$\max \langle |\mathbf{v}_\perp| \rangle_z$	(L, M, N_r)
0	1251 ± 1	1629 ± 3	0.491	0.384	1.000	0.000	0.70	0.057	-0.31	0.019	$(7, 10, 30)$
0.5	1481 ± 1	1567 ± 1	0.485	0.387	0.818	0.089	0.67	0.062	-0.33	0.019	$(7, 10, 30)$
1	2028 ± 3	1638 ± 3	0.458	0.378	0.614	0.143	0.61	0.062	-0.39	0.019	$(9, 12, 34)$
2	3769 ± 9	2016 ± 5	0.480	0.395	0.429	0.120	0.61	0.055	-0.42	0.011	$(7, 10, 30)$

Table 2: For $m_0 = 3$, $q_0 = 2.44$, properties of the critical wave solutions shown by the disks in Fig. 8. The third column is the corresponding value of the pressure gradient Reynolds number. The symbol $\delta\mu_W$ is defined in Eq. (70). The max and min in the following columns are taken with respect to r and θ. The last column indicates the truncation levels used for the computations.
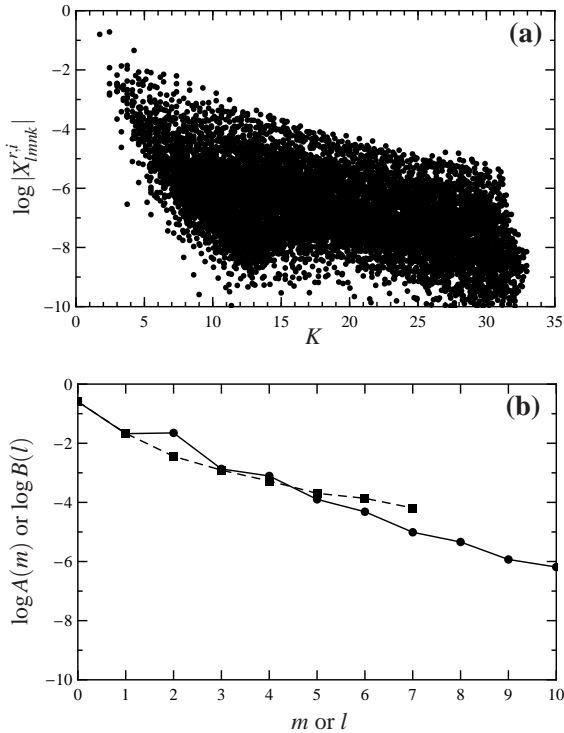

Figure 10: Spectrum of the critical wave in the Newtonian case $\lambda = 0$. (a) : Decimal logarithms of the 9398 coefficients $|a_{lmnk}^{r,i}| > 10^{-10}$ vs the generalized wavenumber K defined by Eq. (58). (b) : The disks (resp. squares) show $\log A(m)$ vs m (resp. $\log B(l)$ vs l) with the amplitudes defined by Eqs. (59) and (60).

Figure 11: Same as Fig. 10, but in the non-Newtonian case $\lambda = 2$. In (a) there are 9442 coefficients $|a_{lmnk}^{r,i}| > 10^{-10}$.

in the spectrum for $\lambda = 2$ (Fig. 11b).

to become roughly constant in a larger and larger region near the axis. This effect is essentially due to the base flow contribution (see the Fig. 6a), since it is not visible on the plots of $\langle w \rangle_z$ (right column of Fig. 12). On these plots one notices the presence of fast streaks near the pipe wall, which may be explained by the presence of 3 pairs of counter-rotating vortices visible in the cross-stream fields. Indeed these vortices transport some rapidly moving fluid in the region of the axis towards the walls. A remarkable effect is the transition from 6 fast streaks, in Figs. 12a and b, for $\lambda = 0$ and 1, to 3 fast streaks, in Fig. 12c, for $\lambda = 2$. For $\lambda = 0$, 6 fast streaks are also visible in the Fig. 13a of [13], which we have been able to reproduce. The transition from 6 to 3 fast streaks can be seen as a consequence of a spatial broadening of the cross-stream outflows associated with the cross-stream vortices, as visible in Fig. 13. The fact that one has 6 fast streaks for $\lambda = 0$ vs 3 fast streaks for $\lambda = 2$ is obviously linked to the dominance of the second azimuthal harmonic in the spectrum for $\lambda = 0$ (Fig. 10b) but not
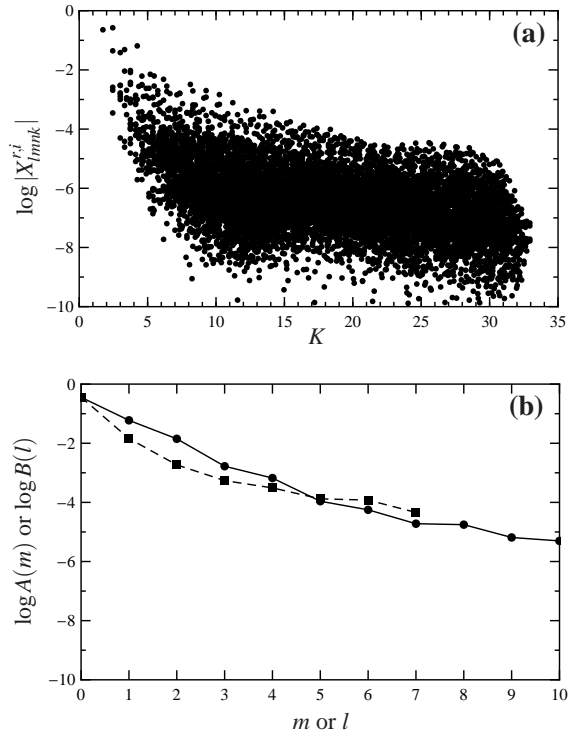
6. Concluding discussion

A Petrov-Galerkin code has been developed. It is similar, in his principles, to the code of Meseguer and collaborators, especially to the Newton-Krylov version used in [27, 28]. However, a major difference is the encoding of a nonlinear viscosity that depends on the velocity field according to Eqs. (4) and (5). This required a special care at the level of the Newton-GMRES method, as explained in our Sec. 3.5. This code has been validated and its convergence properties have been studied. Spectral convergence is obtained, despite of the highly nonlinear nature of the relation between the viscosity and the velocity components.

The main physical result of this work is the stabilizing influence of shear-thinning effects on the nonlinear waves that may support the turbulent puffs in pipe flow. As shown in the first columns of Tab. 2, the stabilization for the wave with the critical wavenumbers for the Newtonian case ($m_0 = 3$ and $q_0 = 2.44$)
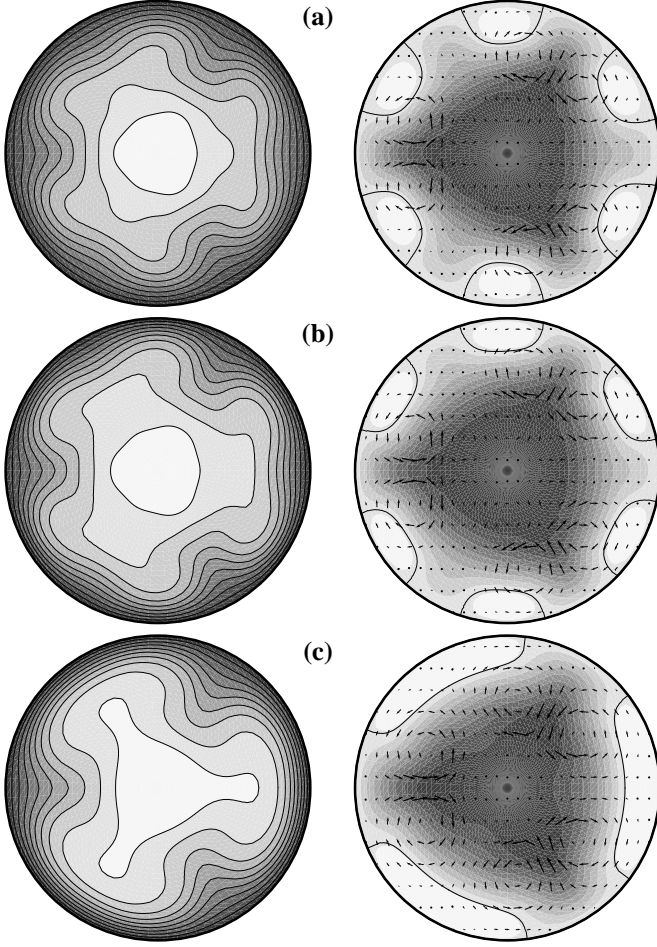
Figure 12: Visualization of the velocity field of the critical waves averaged in the axial direction, for (a) $\lambda = 0$, (b) $\lambda = 1$, (c) $\lambda = 2$. Left: contours of the axial velocity $\langle v_z \rangle_z$; the contour steps are $(\max \langle v_z \rangle_z)/10$. Right: axial velocity difference $\langle w \rangle_z = \langle v_z - W_b \rangle_z$ and arrows showing the cross-stream velocity field $\langle \mathbf{v}_\perp \rangle_z = \langle u \rangle_z \mathbf{e}_r + \langle v \rangle_z \mathbf{e}_\theta$. The contour steps for the axial velocity are $(\max \langle w \rangle_z - \min \langle w \rangle_z)/10$. The contour line $\langle w \rangle_z = 0$ is drawn. In the grayscale plots dark regions denote slow velocities whereas clear regions denote high velocities.

is moderate in terms of the pressure-gradient Reynolds number Re: the transition is delayed from $Re(0) \simeq 1630$ in the Newtonian case $\lambda = 0$ to $Re(2) \simeq 2020$ in the non-Newtonian case $\lambda = 2$. However, the transition delay becomes substantial when the wall-viscosity Reynolds number $\overline{Re}_W$, which is more relevant for non-Newtonian fluids (Sec. 2.5), is used. In terms of $\overline{Re}_W$, the transition is delayed from $\overline{Re}_W(0) = \overline{Re} \simeq 1250$ in the Newtonian case $\lambda = 0$ to $\overline{Re}_W(2) \simeq 3770$ in the non-Newtonian case $\lambda = 2$. It is our conviction that this delay is related to the experimental results mentioned in Introduction.

The delay factor, the ratio of the two Reynolds numbers,

$$\frac{\overline{Re}_W(\lambda)}{\overline{Re}_W(0)} \simeq \frac{1}{\mu_W(\lambda)} \frac{Re(\lambda)}{Re(0)} \tag{71}$$

because the flow rates are similar in the Newtonian and non-Newtonian waves. The role of the ratio $1/\mu_W$ between the viscosity at zero strain and the wall-viscosity ($1/\mu_W = 2.365$ in the case $\lambda = 2$, according to the Tab. 1) is remarkable. It would
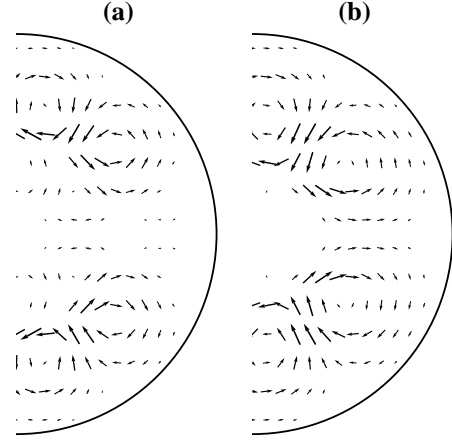

Figure 13: Cross-stream velocity fields in one half of the pipe for (a) $\lambda = 0$, (b) $\lambda = 2$. On a regular grid, only the vectors with $|\langle \mathbf{v}_\perp \rangle_z| > \frac{1}{10} \max |\langle \mathbf{v}_\perp \rangle_z|$ are shown.

be interesting to extend these computations to higher values of the non-Newtonian parameter λ, to see if the ratio $Re(\lambda)/Re(0)$ continues to increase with λ for $\lambda > 2$, which would lead to a very strong stabilization at large λ in terms of the ratio $\overline{Re}_W(\lambda)/\overline{Re}_W(0)$. This regime of large λ is the experimentally relevant one. Indeed, the inversion of the Eqs. (34), where we consider that approximately $2 \langle v_z \rangle_{r\theta} \simeq 1$, and (67), yields

$$\lambda = \frac{\hat{\mu}_0 \hat{\lambda}}{\hat{\rho} \hat{a}^2} Re \simeq \frac{\hat{\mu}_0 \hat{\lambda}}{\hat{\rho} \hat{a}^2} \mu_W \overline{Re}_W . \tag{72}$$

For the case of 0.125% PAA studied in [7], the factor

$$\frac{\hat{\mu}_0 \hat{\lambda}}{\hat{\rho} \hat{a}^2} \simeq 77 , \tag{73}$$

whereas a laminar computation such as the ones presented in Sec. 5.1, yields, for a typical wall-viscosity Reynolds number $\overline{Re}_W = 6000$, a value of the wall-viscosity $\mu_W \simeq 0.004$. This corresponds, according to Eq. (72), to

$$\lambda \simeq 1900 . \tag{74}$$

Preliminary studies for $\lambda > 2$ show that high truncation levels, more precisely high values of N_r, may have to be used in such cases, which could pose practical problems, notably in terms of memory capacity. In order to overcome this difficulty, a matrix-free version of the code (with, for instance, a SOR preconditioning) might be developped, since storing the matrices implied in Equation (51) explains most of the memory use (cf. the discussion in Section 3.7).

Another relevant question that will be less difficult to solve is the influence of the azimuthal and axial wavenumbers. A study of this influence will be the object of a forthcoming paper.

Appendix A. Trial and test fields

The choice of the trial and test fields has been discussed in [2, 20]. For the purpose of completeness, we list these functions here. They are defined in terms of the functions

$$h_n(r) = (1 - r^2) T_{2n-2}(r) , \quad g_n(r) = (1 - r^2) h_n(r) \tag{A.1}$$

with T_n the Chebyshev polynomial of degree n, and of the operators

$$D = \frac{d}{dr}, \quad D_+ = D + \frac{1}{r}. \tag{A.2}$$

Appendix A.1. Trial fields

In the case $m = 0$,

$$
\begin{aligned}
\mathbf{V}_{l,0,n,1} &= rh_n\mathbf{e}_\theta, \\
\mathbf{V}_{l,0,n,2} &= -ilrg_n\mathbf{e}_r + D_+(rg_n)\mathbf{e}_z,
\end{aligned} \tag{A.3}
$$

except that, if $l = 0$,

$$\mathbf{V}_{0,0,n,2} = h_n\mathbf{e}_z. \tag{A.4}$$

In the case $m \neq 0$,

$$
\begin{aligned}
\mathbf{V}_{l,m,n,1} &= -imr^{\sigma-1}g_n\mathbf{e}_r + D(r^\sigma g_n)\mathbf{e}_\theta, \\
\mathbf{V}_{l,m,n,2} &= -ilr^{\sigma+1}h_n\mathbf{e}_\theta + imr^\sigma h_n\mathbf{e}_z,
\end{aligned} \tag{A.5}
$$

with $\sigma = \sigma(m) = 1$ if m is odd, 2 if m is even.

Appendix A.2. Test fields

They are all proportional to the Chebyshev weight function

$$W = 1/\sqrt{1-r^2}. \tag{A.6}$$

In the case $m = 0$,

$$
\begin{aligned}
\widetilde{\mathbf{V}}_{l,0,n,1} &= Wh_n\mathbf{e}_\theta, \\
\widetilde{\mathbf{V}}_{l,0,n,2} &= W\{-ilqr^2g_n\mathbf{e}_r + [D_+(r^2g_n) + r^3h_n]\mathbf{e}_z\},
\end{aligned} \tag{A.7}
$$

except that, if $l = 0$,

$$\widetilde{\mathbf{V}}_{0,0,n,2} = Wrh_n\mathbf{e}_z. \tag{A.8}$$

In the case $m \neq 0$,

$$
\begin{aligned}
\widetilde{\mathbf{V}}_{l,m,n,1} &= W\{-imr^\beta g_n\mathbf{e}_r + [D(r^{\beta+1}g_n) + r^{\beta+2}h_n]\mathbf{e}_\theta\}, \\
\widetilde{\mathbf{V}}_{l,m,n,2} &= W(-ilr^{\beta+2}h_n\mathbf{e}_\theta + imr^{\beta+1}h_n\mathbf{e}_z),
\end{aligned} \tag{A.9}
$$

except that, if $l = 0$,

$$\widetilde{\mathbf{V}}_{0,m,n,2} = Wimr^{1-\beta}h_n\mathbf{e}_z. \tag{A.10}$$

In these last Eqs., $\beta = \beta(m) = 1$ if m is odd, 0 if m is even.

References

[1] Hof B, de Lozar A, Kuik DJ, Westerweel J. Repeller or Attractor? Selecting the Dynamical Model for the Onset of Turbulence in Pipe Flow. Phys Rev Lett 2008;101:214501, 1–4.

[2] Meseguer A, Trefethen LN. Linearized pipe flow to Reynolds number 10^7. J Comput Phys 2003;186:178–97.

[3] Wygnanski I, Champagne F. On transition in a pipe. Part 1. The origin of puffs and slugs and the flow in a turbulent slug. J Fluid Mech 1973;59:281–335.

[4] Wygnanski I, Sokolov M, Friedman D. On transition in a pipe. Part 2. The equilibrium puff. J Fluid Mech 1975;69:283–304.

[5] Escudier MP, Presti F, Smith S. Drag reduction in the turbulent pipe flow of polymers. J Non-Newtonian Fluid Mech 1999;81:197–213.

[6] Escudier M, Poole R, Presti F, Dales C, Nouar C, Desaubry C, et al. Observations of asymmetrical flow behaviour in transitional pipe flow of yield-stress and other shear-thinning liquids. J Non-Newtonian Fluid Mech 2005;127:143–55.

[7] Escudier MP, Rosa S, Poole RJ. Asymmetry in transitional pipe flow of drag-reducing polymer solutions. J Non-Newtonian Fluid Mech 2009;161:19–29.

[8] Rudman M, Blackburn HM, Graham LJW, Pullum L. Turbulent pipe flow of shear-thinning fluids. J Non-Newtonian Fluid Mech 2004;118:33–48.

[9] Waleffe F. Three-dimensional coherent states in plane shear-flows. Phys Rev Lett 1998;81:4140–3.

[10] Faisst H, Eckhardt B. Traveling waves in pipe flow. Phys Rev Lett 2003;91:224502, 1–4.

[11] Busse FH. Visualizing the dynamics of the onset of turbulence. Science 2004;305:1574–5.

[12] Hof B, van Doorne CWH, Westerweel J, Nieuwstadt FTM, Faisst H, Eckhardt B, et al. Experimental observation of nonlinear traveling waves in turbulent pipe flow. Science 2004;305:1594–8.

[13] Wedin H, Kerswell RR. Exact coherent structures in pipe flow: travelling wave solutions. J Fluid Mech 2004;508:333–71.

[14] Pringle CCT, Kerswell RR. Asymmetric, helical, and mirror-symmetric traveling waves in pipe flow. Phys Rev Lett 2007;99:074502,1–4.

[15] Pringle CCT, Duguet Y, Kerswell RR. Highly symmetric traveling waves in pipe flow. Phil Trans Roy Soc London A 2009;367:457–72.

[16] Duguet Y, Willis AP, Kerswell RR. Transition in pipe flow: the saddle structure on the boundary of turbulence. J Fluid Mech 2008;613:255–74.

[17] Carreau JP. Rheological equations from molecular network theories. J Rheol 1972;16:99–127.

[18] Yasuda K, Armstrong RC, Cohen RE. Shear flow properties of concentrated solutions of linear and star branched polystyrenes. Rheol Acta 1981;20:163–78.

[19] Nouar C, Bottaro A, Brancher J. Delaying transition to turbulence in channel flow : Revisiting the stability of shear thinning fluids. J Fluid Mech 2007;592:177–94.

[20] Meseguer A, Mellibosky F. On a solenoidal Fourier-Chebyshev spectral method for stability analysis of the Hagen-Poiseuille flow. App Num Math 2007;57:920–38.

[21] Saad Y, Schultz MH. GMRES: a generalized minimal residual algorithm for solving nonsymmetric linear systems. SIAM J Sci Stat Comput 1986;7:856–69.

[22] Eisenstat SC, Walker HF. Choosing the forcing terms in an inexact Newton method. SIAM J Sci Stat Comput 1996;17:16–32.

[23] Walker HF. Implementation of the GMRES method using Householder transformations. SIAM J Sci Stat Comput 1988;9:152–63.

[24] Keller HB. Numerical solution of bifurcation and nonlinear eigenvalue problems. In: Rabinowitz PH, editor. Applications of Bifurcation Theory. Academic Press; 1977, p. 359–84.

[25] Walker HF. An adaptation of Krylov subspace methods to path following problems. SIAM J Sci Stat Comput 1999;21:1191–8.

[26] Severac E, Serre E. A spectral vanishing viscosity for the LES of turbulent flows within rotating cavities. J Comput Phys 2007;226:1234–55.

[27] Meseguer A, Avila M, Mellibovsky F, Marques F. Solenoidal spectral formulations for the computation of secondary flows in cylindrical and annular geometries. Eur Phys J Special Topics 2007;146:249–59.

[28] Mellibovsky F, Meseguer A. Critical threshold in pipe flow transition. Phil Trans R Soc A 2009;367:545–60.